Journal of the European Ceramic Society 44 (2024) 784–794

Contents lists available at ScienceDirect

Journal of the European Ceramic Society

journal homepage: www.elsevier.com/locate/jeurceramsoc

Original article

Obtaining SiC Fibers–PyC interfacial properties through push-out FEM Models

Alvaro Martinez-Pechero [a,*], Yevhen Zayachuk [b], Anna Widdowson [b], David E.J. Armstrong [c], Edmund Tarleton [a,c]

[a] Department of Engineering Science, University of Oxford, Parks Road, Oxford, OX1 3PJ, Oxfordshire, UK
[b] UK Atomic Energy Authority, Culham Science Centre, Abingdon, OX14 3EB, Oxfordshire, UK
[c] Department of Materials, University of Oxford, Parks Road, Oxford, OX1 3PH, Oxfordshire, UK

ARTICLE INFO

Keywords:
SiC fibers
Push-out
Nanoindentation
Cohesive zone model

ABSTRACT

Silicon carbide (SiC) has attractive properties for use in nuclear reactors. However, it is hampered by inherent brittleness that is overcome through a fiber-reinforced composite. A finite element model based on cohesive zone contact coupled to Coulomb friction is proposed to simulate the push-out response of isolated fibers in SiC/PyC fiber-reinforced composites. The model reproduces the measurements obtained during push-out experiments of isolated fibers in different configurations and predicts interfacial failure between the PyC interphase and fiber. The brittle properties predicted coincide with literature indicating that fiber–PyC interface could prevent the crack propagation through the fiber, fulfilling the function of the structure.

1. Introduction

Silicon carbide (SiC) possesses many attractive properties to be a structural material, able to withstand extreme temperature environments such as nuclear fission [1] or fusion [2] reactors, or aerospace applications [3]. These characteristics include low density [3], good oxidation resistance [4], high-temperature tolerance, and creep resistance [5].

However, its practical use is hampered by inherent brittleness [6]. To overcome this, the structure of a continuous SiC fiber-reinforced composite has been proposed [7].

The fiber composite technique consists of growing a SiC matrix over a structure of woven or braided reinforcing SiC fibers. In this way, when a crack grows it is deflected upon contact with the fibers, leaving them undamaged thus reinforcing the overall structure. The friction between the matrix and the undamaged fibers reduces the crack separation increasing the toughness of the composite and leading to pseudo-ductile behavior.

The study of the fiber–matrix interphase material and its contact area with the fiber, known as the interface is fundamental to evaluate the role of fibers in crack resistance. For nuclear applications, pyrolytic carbon (PyC) is the material chosen for the interphase due to its resistance to moderate irradiation effects [8].

Various experimental methods have been suggested for the characterization of the fiber–matrix interphase such as micropillar compression [9], micro-cantilever fracture [10] and fiber push-out [11].

Flat-tip push-out studies the role of friction and mode II cracks at the interphase maintaining the fiber integrity. However, it requires in-depth analysis for proper interpretation due to the complexity of the experiment. Compression of the fiber causes swelling in the radial direction producing friction that compensates for the loss of overall stiffness and slows down crack propagation. The load grows to a peak where interphase cracking is complete and the resistance drops to a plateau region where friction dominates [12]. The nonlinearity of the process requires complex analytical models [13].

Numerous push-out experiments have been extensively documented in the literature [11,14–16]. Some studies have highlighted significant variations in fiber attachment strength based on different factors, including the fiber nature (SA3 or NHS), interphase structure (monolayer or multilayer), PyC structure (isotropic or anisotropic) [14,16], and interphase roughness (highly irregular [15] or flat [11]). However, it is worth noting that differentiating between the interphase link force and the resistance caused by friction is a seldomly explored aspect in push-out experiments [14,15]. Existing studies have utilized simplified formulations [13], neglecting the influence of PyC toughness and gradual crack propagation. In this context, numerical models can play an important role in discerning the contributing factors affecting fiber resistance during push-out, thereby providing valuable physical insights that may not be readily measurable in experimental settings.

This contribution presents a Finite element model of two push-out experiments. Crack modeling is based on a cohesive zone model in

---

[*] Corresponding author at: Department of Engineering Science, University of Oxford, Parks Road, Oxford, OX1 3PJ, Oxfordshire, UK.
E-mail address: alvaro.martinezpechero@eng.ox.ac.uk (A. Martinez-Pechero).

https://doi.org/10.1016/j.jeurceramsoc.2023.09.080
Received 27 February 2023; Received in revised form 8 September 2023; Accepted 29 September 2023

combination with Coulomb friction. The material studied was a SiC sample produced by chemical vapor infiltration (CVI) [17] reinforced by Tyranno SA3 fibers which are separated by a PyC interphase and the push-out was performed in a bridge configuration [18].

The model parameters were obtained from the experiments and literature with a margin of uncertainty depending on measurements and references. To compensate this, push-out experiments were repeated at different positions of the bridge and an optimization algorithm was applied to identify the combination of parameters that best fit the set of measurements.

Finally, the role of friction in crack propagation and the viability of PyC for crack deflection were studied. Based on push-out theory [13], some precautions in the way of calculating the interfacial shear strength were proposed to improve the accuracy of the measurements.

2. Push-out experiments

In this section, we discuss the details related to the fabrication, properties and push-out experiments of the Tyranno SA3 fiber-reinforced composite.

2.1. Fiber-reinforced ceramic composites

There are many techniques of manufacturing SiC fiber-reinforced matrix such as melt infiltration [19], polymer infiltration and pyrolysis (PIP) [1], transient eutectic phase (TEP) [20] and chemical vapor infiltration (CVI) [17].

In the sample, the matrix was produced via the CVI technique. A gaseous SiC precursor as methyl trichlorosilane (CH3SiCl3) is mixed with hydrogen and introduced into a high-temperature chamber where the prefabricated fiber structure is located. The precursor decomposes in the presence of hydrogen and the gas-phase pyrolysis products chemically react with the substrate forming a silicon carbide matrix within and around the fiber reinforcement [21]. CVI has the advantage of being able to produce very high purity β-phase SiC that exhibits good radiation resistance [22], making it suitable for nuclear cladding. However, the process might require several weeks of infiltration time and leaves a large porosity.

The sample studied contains Tyranno SA3 fibers (Ube Industries Ltd), characterized by their low oxygen concentration which reduces creep and rupture mechanisms at high temperatures [23]. Fibers are uniformly coated with one interphase made of ~100 nm PyC using the chemical vapor deposition (CVD) technique [7].

The sample was cut with a Capco diamond saw, obtaining a bar of 10 mm × 1 mm × 0.7 mm with fiber bundles parallel and perpendicular to the surface. It was then mechanically ground with SiC grinding discs on the front and back surfaces to a final thickness of ~ 80 μm, and polished with diamond suspension of 3-1 μm grain size. The sample was clamped forming a 3 mm length bridge configuration (see Fig. 1).

2.2. Fibers and PyC interphase

The fibers have a small diameter (7–9 μm) and are distributed in bundles with higher fiber density and porosity in the center than in the periphery where the matrix is more homogeneous (see Fig. 2), being the fibers in the periphery the ones selected for the measurements in order to avoid undesired porosity effects [11].

Zayachuk et al. [10] present the structure of the fiber as an agglomeration of equiaxed grains of size between 50–200 nm. The grain size of the fibers is radially non-uniform and increases towards the fiber periphery. On the other hand, the concentration of carbon inclusions decreases from the center towards the periphery. This structure affects the elastic modulus of the fiber which increases linearly from E = 250 GPa in the center of the fiber up to E = 450 GPa towards the periphery. The Poisson's ratio was assumed constant ν = 0.17 [24].

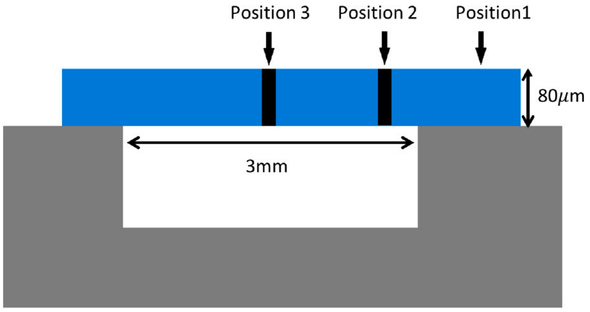

Fig. 1. Bridge configuration of the sample and positions where experiments were performed.

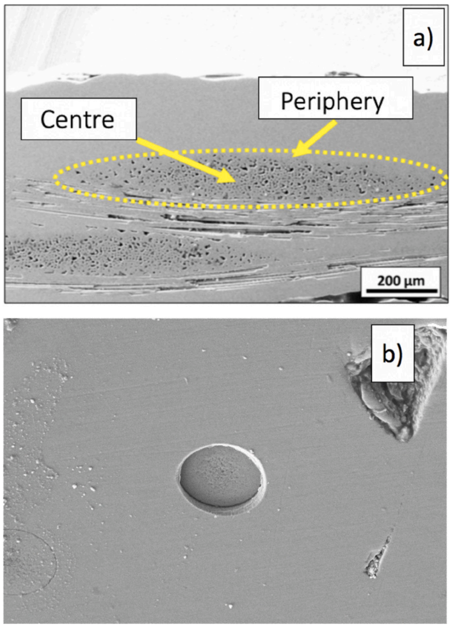

Fig. 2. (a) Left image: Bundle of fibers with higher density in the center than in the periphery. (b) Example of periphery fiber used in the push-out experiment because is isolated from other fibers and pores.

The fibers are surrounded by a ~100 nm PyC interphase that protects them from crack propagation in the matrix. The contact area between the fiber and the PyC interphase is known as the PyC–fiber interface. Push-out cracks may occur in the PyC interphase or the PyC–fiber interface [25].

In other similar samples, SEM images of push-out tests [11] showed no PyC deposits on the SA3 fibers, which is a good indicator that the crack did not occur across the PyC interphase. In addition, TEM images of a crack in a cantilever of the same material [10] showed a clear failure in the interface. There is no information about some crack properties of the interface, however some approaches such as molecular dynamics simulations [26] or theoretical fracture mechanics [27] provide information about the range of values of these magnitudes, which are subsequently adjusted using the FEM results and the experiments.

2.3. Push-out measurements

Push-out measurements were performed using an Agilent XP nanoindenter and a flat-punch indenter tip with a diameter of ~5.4 μm. It was equipped with an x40 optical objective, capable of resolving

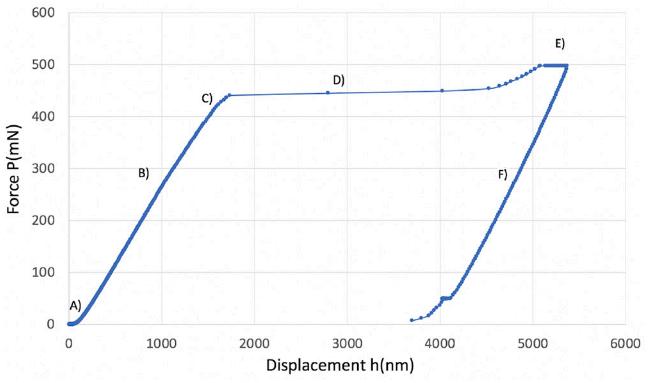

Fig. 3. Stages of the curve during push-out experiments.

individual fibers, and a movable stage to accurately place fibers under the indenter. Measurements were performed in a load-controlled mode with a constant strain rate of 0.05 s^{-1}. Experimental measures of space dimensions and Young's modulus of the matrix with the margins of error are presented in Table A.1.

The curves resulting from the push-outs are characterized by several phases shown in Fig. 3:

(A) Initial quasi-flat region corresponding to the approach of the tip to the fiber and its adaptation to the roughness of the surface.
(B) Linear-elastic region, the indenter produces a response similar to matrix nanoindentation.
(C) Crack initiation at the interface. It is difficult to determine when a crack initiates and its evolution, the reduction of stiffness due to crack initiation is compensated by fiber expansion and friction presenting a small reduction in the load–displacement slope curve.
(D) Plateau load regime occurs after the crack has been propagated across the interface and the sample stiffness drops. Traditional push-outs models [28,29] illustrate a peak load followed by an abrupt drop. In our experiments, we use a load control indenter and once the debonded fiber moves abruptly we cannot control the load for each displacement, being represented by a plateau with a similar load.
(E) After the complete debonding of the fiber, the lateral edges of the tip, which has a shape of a truncated cone, touch the edges of the hole left by the fiber producing an additional increase in the load.
(F) The unloading regime does not provide any physical information.

Our models are focused in the elastic and crack propagation regime which corresponds to (B) and (C).

3. Finite element models

The need to model the behavior of the fibers in a ceramic composite during a crack in its structure led us to use Finite Element Modeling (FEM) because of its flexibility to represent these complex processes. Abaqus 2021 [30] was used as the FEM software for the simulations.

The models were designed to reproduce the flat-tip nanoindentation experiments in three positions of the ceramic matrix composite: $P1$: matrix area resting on a support of the bridge, $P2$: matrix area suspended but not in the center of the bridge, $P3$: central section of the suspended matrix area, see Fig. 1.

Two types of FEM simulations were performed: *Elastic Models of SiC matrix* to characterize the parameters of the matrix and *Cohesive Zone Models* to characterize the behavior of the interface during fiber push-out experiments.

3.1. Elastic models of SiC matrix

Initially, the impact of tip compression was studied. For this purpose, a model with a virtual diamond flat tip and another model without a flat tip but imposing a homogeneous displacement boundary condition in the indentation zone were compared on $P1$, Fig. B.9.

Due to the cylindrical symmetry of $P1$, ∼85 000 8-node biquadratic axisymmetric quadrilateral elements (CAX8) were employed to model the virtual tip and the sample made of SiC matrix material. Both parts were joined via rough contact formulation. The results of this model were compared with a 3D model using ∼120,000 20-node quadratic brick fully integrated elements (C3D20) and homogeneous displacement-control load Fig. B.9.

Once it was verified that the results of both boundary conditions were equivalent, the displacement-control was used for simplicity to characterize the matrix parameters in $P2$ and $P3$.

$P3$ was simulated with a 1/4 of the sample (using ∼180,000 C3D20 elements) because it is symmetric in the bridge according to length and width. $P2$ was simulated with 1/2 of the sample (using ∼200,000 C3D20 elements) because it is symmetric only in width but not in length due to not being in the center of the bridge, (see Fig. 1).

3.2. Cohesive zone model (CZM)

Push-out experiments produce mode II crack propagation in the PyC–fiber interface [10,11]. A cohesive zone model (CZM) coupled with Coulomb friction has been adopted to represent this failure behavior. The cohesive zone model consists of a constitutive relation between the tractions acting on the interface and the corresponding interfacial separation. In the present work, we use a bilinear law [31] as the constitutive relation.

The known direction of the crack propagation and the physical interpretation of the parameters make a cohesive zone model very attractive compared to other methods such as J-integral or XFEM [30]. Furthermore, LAMMPS atomistic simulations [26] demonstrate bilinear traction–separation behavior for mode II cracks formed between the PyC–fiber interface.

A bilinear law can be divided into an elastic undamaged regime, damage-initiation criteria, a damage propagation regime and complete failure criteria. Constitutive equations in the undamaged regime are:

$$\begin{bmatrix}\sigma_n\\ \tau_s\\ \tau_t'\end{bmatrix} = \begin{bmatrix}K_{nn} & K_{ns} & K_{nt}\\ K_{ns} & K_{ss} & K_{st}\\ K_{nt} & K_{st} & K_{tt}\end{bmatrix}\begin{bmatrix}\delta_n\\ \delta_s\\ \delta_t\end{bmatrix} \tag{1}$$

where σ_n is the normal stress, $\tau_{s/t}$ are the shear stress in the two tangential directions, $K_{i,j}$ is the stiffness matrix and δ_i is the nodal displacement in the normal n or tangential directions t and s.

Damage initiation is represented via the quadratic onset criterion:

$$\begin{gathered}\sqrt{\left(\frac{\langle\sigma_n\rangle}{\sigma_I^{\max}}\right)^2 + \left(\frac{\tau_s}{\sigma_{II}^{\max}}\right)^2} = 1\\ \langle\sigma_n\rangle = \sigma_n;\quad \sigma_n > 0\\ \langle\sigma_n\rangle = 0;\quad \sigma_n < 0\end{gathered} \tag{2}$$

where σ_I^{max} and σ_{II}^{max} are the cohesive interface strengths for mode I and II (mode III is ignored for this model because the geometric shape of the crack forming a cylinder).

Once the cohesive damage has initiated, the propagation regime begins. The interface shear stress has contributions from the cohesive model (for mode II) and the friction model (if $\sigma_n < 0$):

$$\begin{gathered}\sigma_n = \begin{cases}(1-D)\bar{\sigma}_n; & \sigma_n > 0\\ \bar{\sigma}_n; & \sigma_n \le 0\end{cases}\\ \tau_s = \begin{cases}(1-D)\bar{\tau}_s; & \sigma_n > 0\\ (1-D)\bar{\tau}_s + D\mu\bar{\sigma}_n; & \sigma_n \le 0\end{cases}\end{gathered} \tag{3}$$

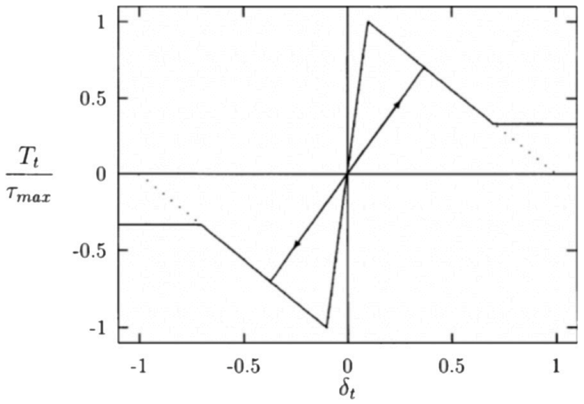

Fig. 4. Representation of mode II bilinear traction–separation law in combination with Coulomb friction [12].

where $\bar{\sigma}_n$ and $\bar{\tau}_s$ are the normal and shear components if the cohesive region were undamaged, in other words, defined by Eq. (1). μ is the Coulomb friction coefficient. The contribution from the friction model is weighted by the cohesive damage variable D, which is 0 when the quadratic onset criterion is accomplished and 1 when the failure is complete.

The complete failure is defined by the linear interaction criterion.

$$\frac{G_I}{G_{IC}} + \frac{G_{II}}{G_{IIC}} = 1, \tag{4}$$

where $G_I = \int \sigma_n d\delta_n$ and $G_{II} = \int \tau_s d\delta_s$ are the energetic work of fracture. Toughness $G_{IC/IIC}$ are material properties obtained experimentally that represent the energy released when failure is complete. After complete failure, friction remains governed by friction Coulomb's law.

A schematic response of the normalized traction–displacement with friction can be observed in Fig. 4. The implementation was done using surface cohesive elements of Abaqus combined with a tangential stiffness penalty. A viscosity coefficient of $\eta = 0.0005$ was introduced to facilitate calculations during the optimization.

Simulations were designed with ~450,000 C3D8 elements for $P3$ and ~650,000 C3D8 elements for $P2$. The boundary conditions are analogous to the elastic models. The fiber elastic properties vary radially and were implemented through a USDFLD subroutine (see Section 2.2).

The residual stress from the previous nanoindentation on the matrix and the thermal stress were neglected due to the lack of experimental measurements. The PyC layer surrounding the cohesive region was neglected in the model because it should not contribute to the global elastic conditions of the interface due its low thickness (~100 nm).

Interface roughness affects the crack propagation and friction [15]. For the sample studied, STEM images indicate a low level of roughness compared to other interphases [11]. The frictional effects are included in the Coulomb friction coefficient and the fracture was negligible (further details in the Appendix C)

3.3. Nelder–Mead optimization

The uncertainty in geometrical parameters (length L, thickness t), and Young's modulus E supposed a difficulty to model the matrix force response in the push-out model (see Table A.1 with the errors).

Nanoindentation in the matrix at $P3$ presents an elastic response that can be expressed by the following equation, showing the high impact of these parameters on the force ($P \propto t^3/L^3$ and $P \propto E^*$):

$$P = \frac{192E^*wt^3h}{12L^3} \quad \frac{1}{E^*} = \frac{(1-\upsilon^2)}{E} + \frac{(1-\upsilon'^2)}{E'} \tag{5}$$

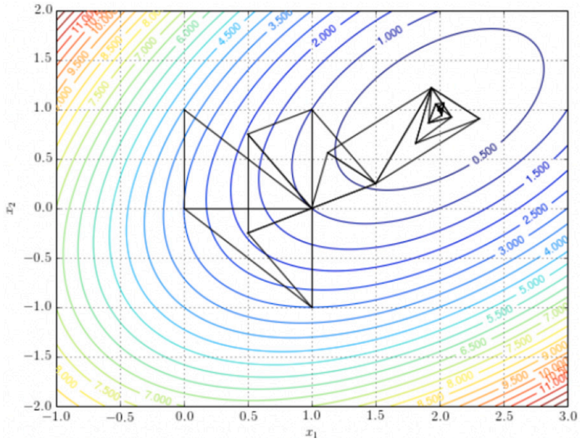

Fig. 5. Nelder–Mead optimization for 2D parameters. Contour lines represent points with equal values of the distance function, the triangles reduce their size while the algorithm approximates to the optimum parameters [33].

P is the load, h the indenter displacement, υ Poisson's ratio, E the Young's modulus, E^* the reduced Young's modulus and w the width of the sample.

With the objective to implement a homogeneous elastic matrix for push-out simulations, a Nelder–Mead [32] optimization algorithm was implemented to identify the combination of values within the margins of errors that best fit the results obtained during matrix nanoindentation in the different positions. Nelder–Mead was chosen between other optimization methods because it converges fast considering the time consumption for FEM simulations and does not require the calculation of the mathematical derivative of the distance function.

Nelder–Mead is a heuristic optimization algorithm where the parameters are adjusted to minimize a distance-function previously defined. It uses a geometrical shape called simplex which corresponds to n-dimensional version of a 'triangle' (n being the number of parameters). Starting with a simplex where one vertex's coordinates correspond to the initial values and the other vertices are randomly generated, it proceeds to reshape/move the simplex, one vertex at a time, towards an optimal region in the search space (Fig. 5). Starting from the experimental data as initial values, the search space was defined by the margins of error of L, t, and E. The optimization algorithm compares the simulation curves with the experimental curves trying to minimize the following distance function.

$$Dist = \max_{i=[2,3]} \left(\frac{\left| a^{exp}_{pos-i} - a^{model}_{pos-i} \right|}{\mid a^{exp}_{pos-i} \mid} \right) \tag{6}$$

where a is the slope of the linear fit of the experimental data (exp) or the Abaqus model (model) and $pos-i$ the different positions used during the optimization.

The algorithm was implemented in R language using the optimx library and a sockets-gateway to communicate with the Abaqus python script that executes the FEM simulations trying to minimize the distance function.

The optimization algorithm progressively converges to a solution but does not guarantee that it is unique. To validate the solution, the algorithm was executed several times with different initial parameters to check the solution converges to similar values.

The same method was applied to find Coulomb friction parameter μ, mode II toughness G_{II} and the shear strength τ_s. In this case, the distance function was defined by the Euclidean distance between the maximum force values. The initial values come from literature [9,26,27].

$$Dist = \max_{i=[2,3]} \left(\frac{(P^{exp} - P^{sim})^2}{(P^{exp})^2} + \frac{(h^{exp} - h^{sim})^2}{(h^{exp})^2} \right) \tag{7}$$

where P is the load peak (mN) and h the nanoindenter displacement (nm).

4. Results and discussion

The objective of this work was to reproduce different nanoindentation and push-out experiments with FEM models to analyze in detail the internal processes of the material.

In the first phase, simulations of nanoindentations were carried out on positions of the matrix without fibers to characterize the properties of the SiC matrix (thickness, length and Young's modulus). Once the matrix was better characterized, fiber push-out models were developed to study in depth the propagation of cracks in a matrix with fibers.

4.1. SiC matrix nanoindentations

The elastic response of the matrix was measured by means of 500 mN flat-tipped nanoindentations on a SiC matrix at different positions: $P1$, $P2$ and $P3$ (see Fig. 1).

To study the impact of tip compression in $P1$, a model with a virtual diamond flat tip was compared with a model where the tip is substituted by a homogeneous displacement load on the indentation zone.

The high stress compresses the diamond tip thereby increasing the measured displacement calculated from the indent. Eq. (8) shows the force–displacement relationship with respect to Young's modulus for a flat tip and Young's modulus adaptation for tip compression.

$$\frac{dP}{dh} = 2E^*\frac{\sqrt{A}}{\sqrt{\pi}} \qquad \frac{1}{E^*} = \frac{\left(1-\nu^2\right)}{E} + \frac{\left(1-\nu_d^2\right)}{E_d} \tag{8}$$

Considering reported values E_d = 1143 GPa, ν_d = 0.07 [34], ν = 0.22 [24] and the ratio dP/dh obtained from the experimental data, it was calculated a ratio E^*/E = 73%, a tip compression of 94 nm for 500 mN and Young's modulus E = 372 GPa, a value that differs 19% from the value measured with a Berkovich tip for the same sample E = 460 GPa [10].

On the other hand, the model with the virtual tip presented a compression of 77 nm (from top to bottom of the tip across the symmetry axis). This compression was compensated in the model with displacement-control load showing both models a similar force–displacement response (see Fig. 6) and similar stress profiles with high-stress concentration at the edges of the contact zone with the tip (see Fig. B.9). These similarities validate continuing the simulations of $P2$ and $P3$ using displacement-control load for simplicity. The models were adjusted to obtain the best fit to experimental data, obtaining E = 392 GPa (14% below E = 460 GPa [10]).

$P2$ and $P3$ nanoindentations were measured to characterize the elastic response of the matrix in a bridge configuration (see Fig. 1), where the bending of the SiC bridge affects a bigger region of the sample than in $P1$. As consequence, the calculation of Young's modulus in $P2$ and $P3$ gave a higher and closer value to the average Young's modulus obtained with the Berkovich tip [10] than $P1$.

Through a Nelder–Mead optimization and successive simulations, the optimum values that best fit the experimental data were obtained: Length = 2884.5 µm (3.8% of deviation from experimental data), thickness = 93.1 µm (16%) and E = 448.5 GPa. (2.5%), see Table A.1 for more details.

$P3$, as a central position in the bridge, could also be compared with the bridge elastic sample equation (Eq. (5)). The slope of the load–displacement curve (Fig. 6) for $P3$ model was P/h = 0.252 mN/nm and using Eq. (5) was P/h = 0.241 mN/nm (4.5% of difference), being a good indicator that the matrix can be approximated to a homogeneous elastic material for posterior push-out modeling.

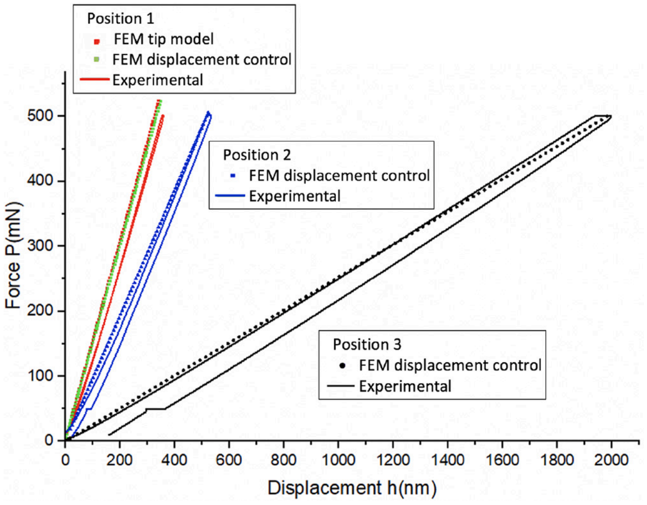

Fig. 6. Nanoindentation load–displacement curves from experiments and FEM for positions 1, 2 and 3 on the SiC matrix.

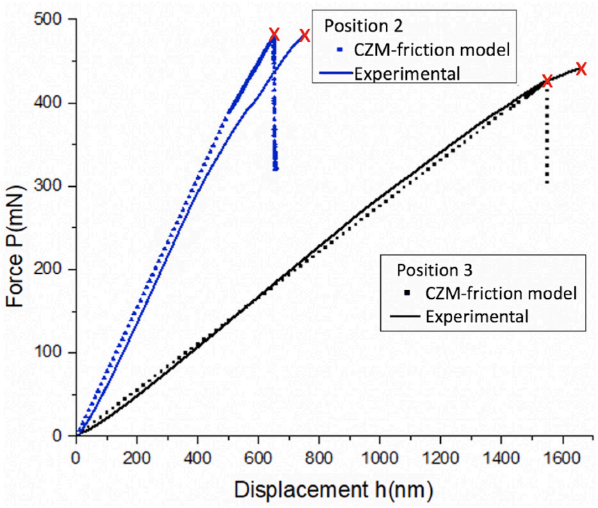

Fig. 7. Push-out load–displacement curves from experiments and models for positions 2 and 3. Red "x" indicates the maximum load reached before the fiber is debonded.

4.2. Fiber push-outs

Results of push-out models at $P2$ and $P3$ are presented in Figs. 8 and B.10 respectively. The Von Mises stress profiles are represented in the lateral, top and bottom profiles of the fiber at different times. In both positions, the initial response is similar to matrix nanoindentations. The sample is bent until the stress at the interface initiates the crack that propagates abruptly from the top to the bottom of the fiber. The loss of stiffness due to cracking is compensated by fiber compression in the z-axis and by Coulomb friction stress due to the fiber expansion in the radial direction. When the crack tip reaches the bottom, the crack is complete and the resistance drops.

In $P2$ (Fig. 8), we can also appreciate how the asymmetric conditions affect the stress profile at the top of the fiber and how the friction is higher on the side closer to the sample attachment. As the crack propagates through the fiber, the asymmetry of the stress profile disappears.

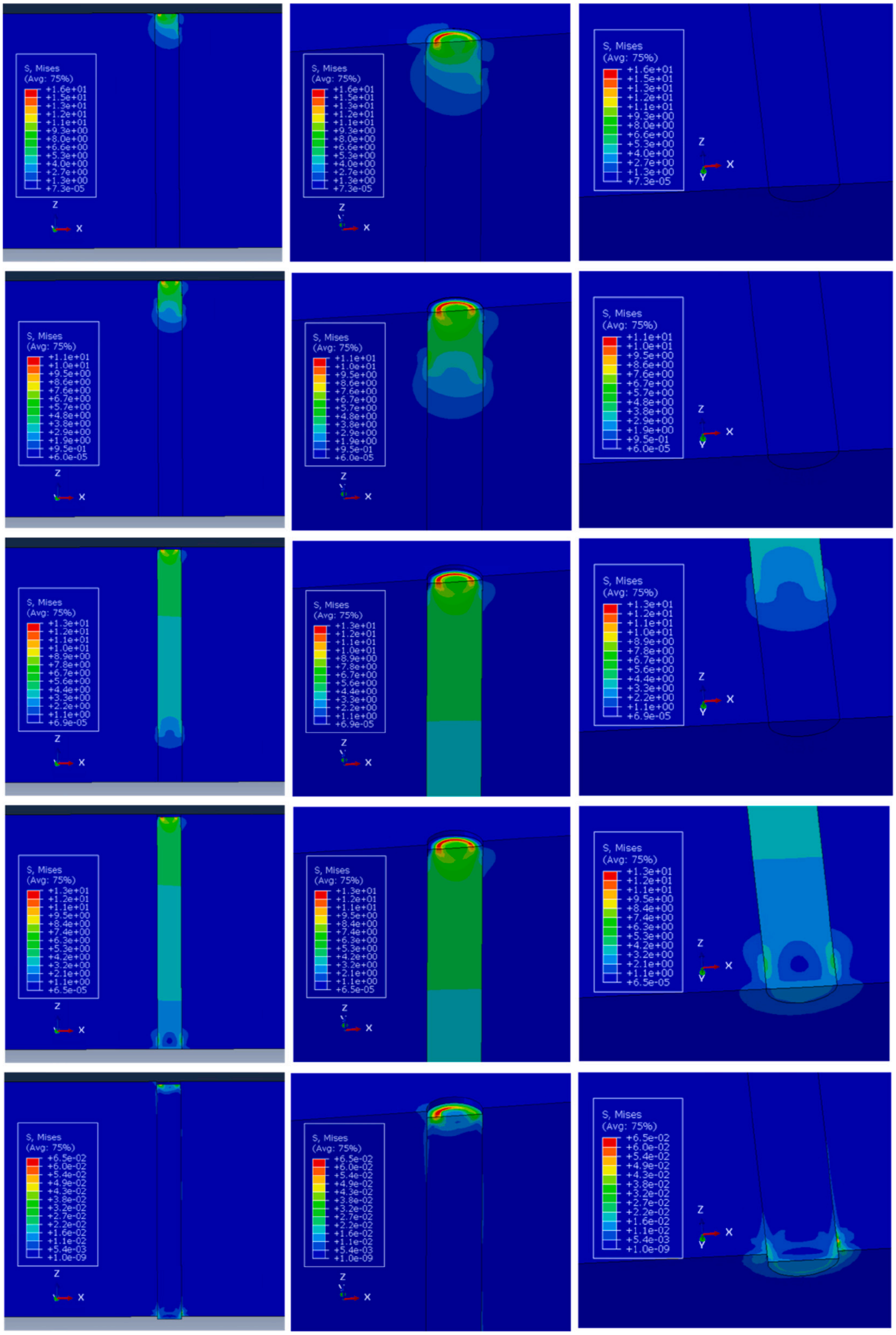

Fig. 8. Von Mises stress propagation in the fiber during crack formation in position 2 from lateral, top and bottom perspective for the same times.

Fig. 7 presents load–displacement curves during $P2$ and $P3$ fibers push-outs. The graph shows a very similar behavior between the experimental results and those obtained in the finite element model based on cohesive zone contact coupled to Coulomb friction.

It can be observed how the force to failure on $P2$ is higher than $P3$, due to the toughening effect of friction, while $P3$ resists more displacement due to the bending of the sample. Experimental curves present a quasi-linear behavior that suggests a brittle interface with high shear strength and catastrophic failure.

The modeling was parameterized with values obtained from the literature. Stiffness $K_n = 2850$ GPa/μm and $K_s = 1150$ GPa/μm for normal and shear stress [26], and shear strength $\tau_n = 3.8$ GPa [26] for crack mode I.

Other parameters with a large impact on the modeling results were adjusted by Nelder–Mead optimization based on values indicated in the literature.

Friction Coulomb coefficient was fitted to $\mu = 0.15$ ($\mu = 0.15$–0.36 according to [9,35]), toughness to $G_I = 5.3$ J/m^2 ($G_I = 2.5$–8.1 J/m^2 according to [9,26]), $G_{II} = 22.3$ J/m^2 ($G_{II} = 10.5$–34 J/m^2 [9,26] calculated as $4.2 \cdot G_I$ [36]) and shear Strength to $\tau_s = 2.1$ GPa for crack mode II ($\tau_s = 1 - 2$ GPa [14,26]).

When a crack occurs, its deflection in the PyC interphase or the PyC–fiber interface protects the fiber from damage and toughens the SiC composite. Lamon et al. [37] exposed two criteria (a, b) to determine if a crack formed in the matrix may be deflected in contact with the PyC interphase or the PyC–fiber interface protecting the fiber from crack propagation.

(a) Deflection at the PyC interphase occurs if $G_{deflection}/G_{propagation} < 0.24$. Although PyC may present a layered crystal structure being highly anisotropic [38], TEM images of similar samples [10] demonstrate that the PyC crystals are randomly oriented, being approximately isotropic in their cracking properties and this criterion is not met.

(b) The criteria for crack deflection at the fiber–PyC interface are $G_{interphase} < 0.25 \cdot G_{fiber} < 4$ J/m^2 [36] or $G_{interphase} < 7$ J/m^2 [37] for $G_{fiber} = 16$ J/m^2 [10]. Both conditions are not satisfied for our experimental data $G_I = 15.7$ J/m^2, a value obtained using Eq. (9) [39] and the stress intensity factor $K_I = 0.8$ MPa m$^{1/2}$ of the PyC–fiber interface measured with a notched cantilever [10] (see Table A.2).

$$G_I = \frac{1-\beta_D^2}{E_*}K_I^2; \quad \frac{1}{E_*} = \frac{1}{2}\left(\frac{1}{E_{PyC}} + \frac{1}{E_{Fiber}}\right) \tag{9}$$

where $\beta_D = 0.26$ is the second Dundur parameter [40] and $E_{PyC} = 12.8$ GPa is the Young modulus of PyC and $E_{Fiber} = 365$ GPa is the Young modulus of the fiber.

However, the (b) criteria is fulfilled for the toughness value of our model $G_I = 5.3$ J/m^2. A possible explanation for the differences between the model values and the experimental values could be that Eq. (9) is designed for planar interface (not the cylindrical shape). Also, the formulas used to obtain the stress intensity factor K_I in [10] are defined for cracks in homogeneous materials instead of interfaces.

The verification of these models will allow them to evolve to characterize the behavior of more complex fiber configurations obtaining the optimum structure before an experimental confirmation.

4.3. Shear strength for high stiffness interfaces

In previous works [11,14–16], the interfacial shear strength τ_s was calculated by the equation:

$$\tau_s = \frac{P}{2\pi Rt} \tag{10}$$

where P is the peak load (i.e., debonding load), R is the fiber radius and t is the sample thickness.

Based on the experimental data, the Eq. (10) gives $\tau_s \sim 0.4$ GPa [11], which differs significantly from the value obtained from simulations $\tau_s \sim 2.1$ GPa. Other simulations based on atomistic codes give $\tau_s = 2.01$ GPa [26]. Zayachuk et al. [10] reported 2.6 GPa using a cantilever made of the same material as our sample. Rebillat et al. [14] reported $\tau_s = 1.3$ GPa in a sample with the same characteristics as our experiments (80 μm thick and 100 nm PyC interphase), a value that could be underestimated since it was taken in the center of the bulk of fibers where porosity and matrix cracking are more frequent.

A possible explanation for these discrepancies could be the fact that Eq. (10) gives the average shear stress across the interface during crack formation, this value would correspond to the shear strength if the entire interface experiences the same shear stress, something that occurs in samples of low thickness or with very flexible interfaces (low stiffness). These differences were studied in recent articles of SiC/PyC/SiC composites [15,16], discerning between the shear strength obtained from Eq. (10) $\tau_s = 0.1$ GPa and the shear strength necessary to break the interface and initiate the fracture which was estimated experimentally $\tau_s = 0.5$–1 GPa.

Fig. 8 presents Von Mises stress in the fiber during crack formation. It can be appreciated how the process is gradual, requiring much lower thickness to accomplish Eq. (10). To overcome this limitation a more general expression is given by [13]:

$$P = \tau_s \frac{\sqrt{a}}{K}\tanh(\sqrt{at})\left(\frac{(1+\nu_{Fiber})}{A_{\text{Fiber}}E_{\text{Fiber}}} - \frac{(1+\nu_{Matrix})}{A_{\text{Matrix}}E_{\text{Matrix}}}\right)^{-1} \tag{11}$$

$$a = 2\pi RK\left(\frac{(1+\nu_{Fiber})}{A_{\text{Fiber}}E_{\text{Fiber}}} - \frac{(1+\nu_{Matrix})}{A_{\text{Matrix}}E_{\text{Matrix}}}\right) \tag{12}$$

where A_i is the cross-sectional area of the fiber and matrix respectively, ν_i is the Poisson's ratio, E_i is Young's modulus and K corresponds to the stiffness of the border between matrix and fiber ($K_s = 1150$ GPa/μm in our case).

Eq. (10) is obtained through the approximation of $\tanh(\sqrt{at}) \sim \sqrt{at}$ when $\sqrt{at} \rightarrow 0$, a condition that is achieved for less stiff interfaces or thinner samples.

In this sample, we obtained $\sqrt{at} = 6.8$ and for $\sqrt{at} > 2$, it is possible to approximate $\tanh(\sqrt{at}) \sim 1$ simplifying calculations to:

$$\tau_s = \frac{PK}{\sqrt{a}}\left(\frac{(1+\nu_{Fiber})}{A_{\text{Fiber}}E_{\text{Fiber}}} - \frac{(1+\nu_{Matrix})}{A_{\text{Matrix}}E_{\text{Matrix}}}\right) \tag{13}$$

We get $\tau_s = 1.8$ GPa, a value closer to $\tau_s = 2.1$ GPa of simulations. Eq. (13) requires detailed knowledge of the fiber, matrix and interfacial properties which are difficult to measure in some cases. Our proposal is not to substitute Eq. (10) by Eq. (13) but to prevent the need to measure push-out peak force with respect to different thicknesses to verify their linear relationship before applying Eq. (10) (when $\tanh(\sqrt{at}) \sim \sqrt{at}$ then P and τ_s are linear in Eq. (11)). Fortunately, recent developments in techniques [41] allow thinner SiC samples, this may overcome the issue exposed and open a new area of more detailed push-out experiments.

5. Conclusions

SiC/PyC fiber-reinforced composite is a promising material to overcome the brittleness of SiC while maintaining its properties. This work studies how PyC interface can be used to protect fibers from crack propagation. Push-out experiments of isolated fibers were done to characterize the fracture process and interface properties. The experiments have been complemented by Finite Element Modeling (FEM) techniques trying to reproduce the results previously obtained in the experiments and provide a detailed analysis of the failure process. The following conclusions can be drawn.

It has been possible to reproduce with good accuracy the experimental behavior of fiber-reinforced SiC using FEM simulations based on a cohesive zone model coupled with friction. Simulations allow us to obtain virtual experiments of the push-outs, easily understandable without the need of complex formulation. The FEM combination with optimization algorithms provides an alternative to experimental data to characterize the properties of the SiC composite such as Young's modulus, shear strength, and toughness of mode I and mode II cracks.

Based on the push-out theory, some recommendations were made for the calculation of interfacial shear strength to avoid incorporating errors of precision when the most common formula is used.

This work can be extended to model other more complex configurations, such as multiple fiber failures over different fiber distributions, and other types of fractures, or adapted to other fiber-reinforced materials.

Table A.1
Dimensions and Young's modulus of the sample and the optimized parameters for the FEM simulations. Measurement errors were obtained from the standard error after different measurements or from the precision of the instruments.

Variable	Experimental measurements	Raw error	%error	Model parameter	% Deviation from experimental
Length (μm)	3000	300	10%	2884.5	3.8%
Thickness (μm)	80	16	20%	93.1	16%
E (GPa)	460	50	10%	448.5	2%
Width (μm)	1000	100	10%	1000	0%
Tip diameter (μm)	5.4	0.2	3%	5.4	0%
Fiber diameter (μm)	8	1	12%	8	0%
PyC interphase (nm)	100	50	50%	–	–
P2 from extreme (μm)	200	20	10%	200	0%

Table A.2
Matrix, fiber, PyC interphase and interface properties from bibliography [10,37,38].

Type	SiC matrix [10]	Fiber [10]	Interface [10]	PyC [37,38]	Interface CZM
E (GPa)	460	250 (center)	38–60	20–35	–
SIF (MPa $m^{1/2}$)	4.25	2	0.8	–	–
G_I (J/m^2)	39	16	15–10	21–34	5.1

Declaration of competing interest

The authors declare that they have no known competing financial interests or personal relationships that could have appeared to influence the work reported in this paper.

Acknowledgments

The authors of this work would like to acknowledge Dr. Riccardo Manno for his support in the FEM. E. Tarleton acknowledges financial support from the Royal Academy of Engineering through a Senior Research Fellowship.

This work has been carried out within the framework of the EUROfusion Consortium, funded by the European Union via the Euratom Research and Training Programme (Grant Agreement No 12490 — EUROfusion) and from the EPSRC (grant number R76251/CN001). To obtain further information on the data and models underlying this paper please contact PublicationsManager@ukaea.uk. Views and opinions expressed are however those of the author(s) only and do not necessarily reflect those of the European Union or the European Commission. Neither the European Union nor the European Commission can be held responsible for them.

Appendix A. Constant tables

See Tables A.1 and A.2.

Appendix B. Finite element models images

See Figs. B.9 and B.10.

Appendix C. Roughness effects in the crack process

In the literature [15], it is discussed the potential influence of interface region roughness on the values of the apparent critical shear stress for debonding.

Although in our case, it can be observed that the 100 nm monolayer of PyC has very low roughness (Fig. C.11a) compared to multilayer samples (Fig. C.11b), preliminary modeling was performed to assess the potential effects of interface roughness variations. For this purpose, push-out simulations were conducted using axisymmetric elements (CAX8, cylindrical coordinates) on a flat interface and a zigzag interface called *wavy interface* (Fig. C.11c), as illustrated in [15]. A zigzag interface was created with displacements of ±200 nm (twice the interphase thickness) in the radial direction for every 2.5 μm in the z-direction over 15 μm-long fibers.

In Fig. C.11e, the stress distribution in the simulation with the *wavy interface* after its rupture can be observed, where the stress impact concentrates in the areas where the interface changes direction causing compression and expansion in different parts of the fiber.

Fig. C.11d presents force–displacement curves comparing simulations on a *flat interface* and a *wavy interface*. In both simulations, a very similar maximum load or shear strength was obtained, indicating that roughness does not seem to have a significant impact on interface fracture or propagation. However, it does have a subsequent effect during fiber sliding, as observed between the blue and orange lines,

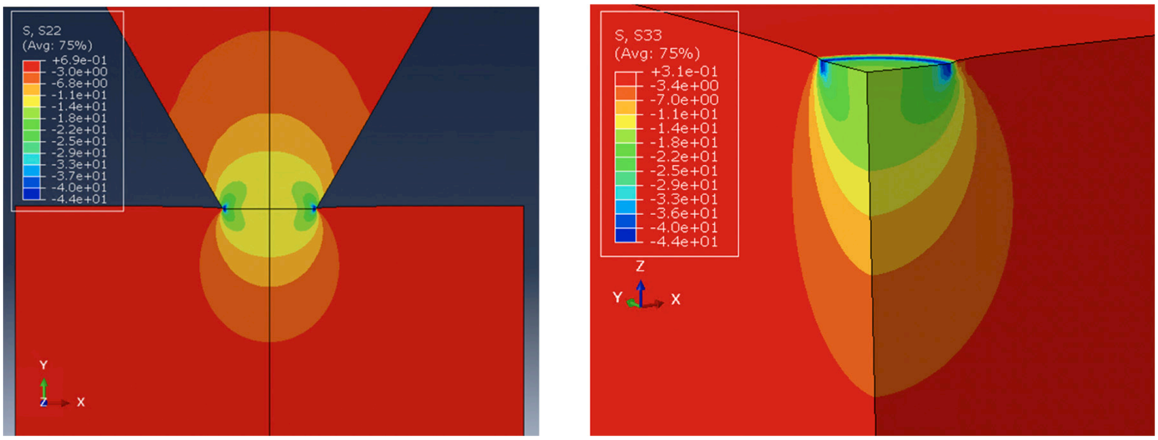

Fig. B.9. (Left) S_{zz} profile at position $P1$ using a flat tip and axisymmetric elements. (Right) S_{zz} profile for 3D model at position $P1$ using homogeneous displacement-control load.

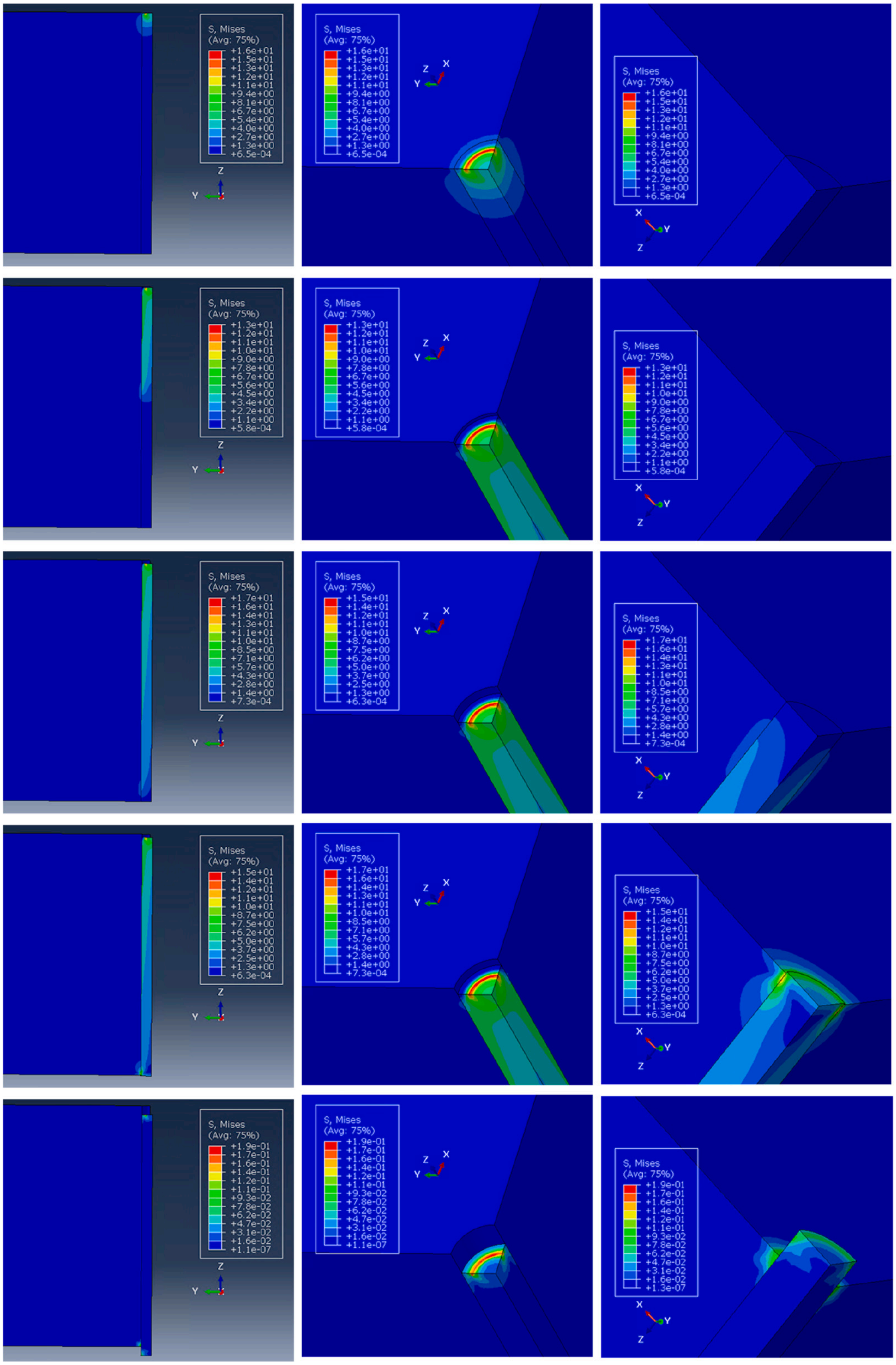

Fig. B.10. Von Mises stress propagation in the fiber during crack formation at position *P*3 from the lateral, top and bottom perspective at the same times.

where fiber widening generates higher friction for the *wavy interface* than for an almost *flat interface*.

In [42], it is studied the roughness profile of a macroscopic fiber (0.8 mm of radius and 5 mm of length). It was found a correlation of 90% between the force necessary to surpass friction P_{fric} and the largest coefficient in the Fourier spectrum of the roughness profile in the interface region, $C_{Fourier}$.

It was obtained P_{fric} of the zigzag interface in two ways; one based on the largest Fourier coefficient of the roughness profile, obtaining $P_{fric}(Fourier) = 107$ mN and the other by FEM simulations obtaining

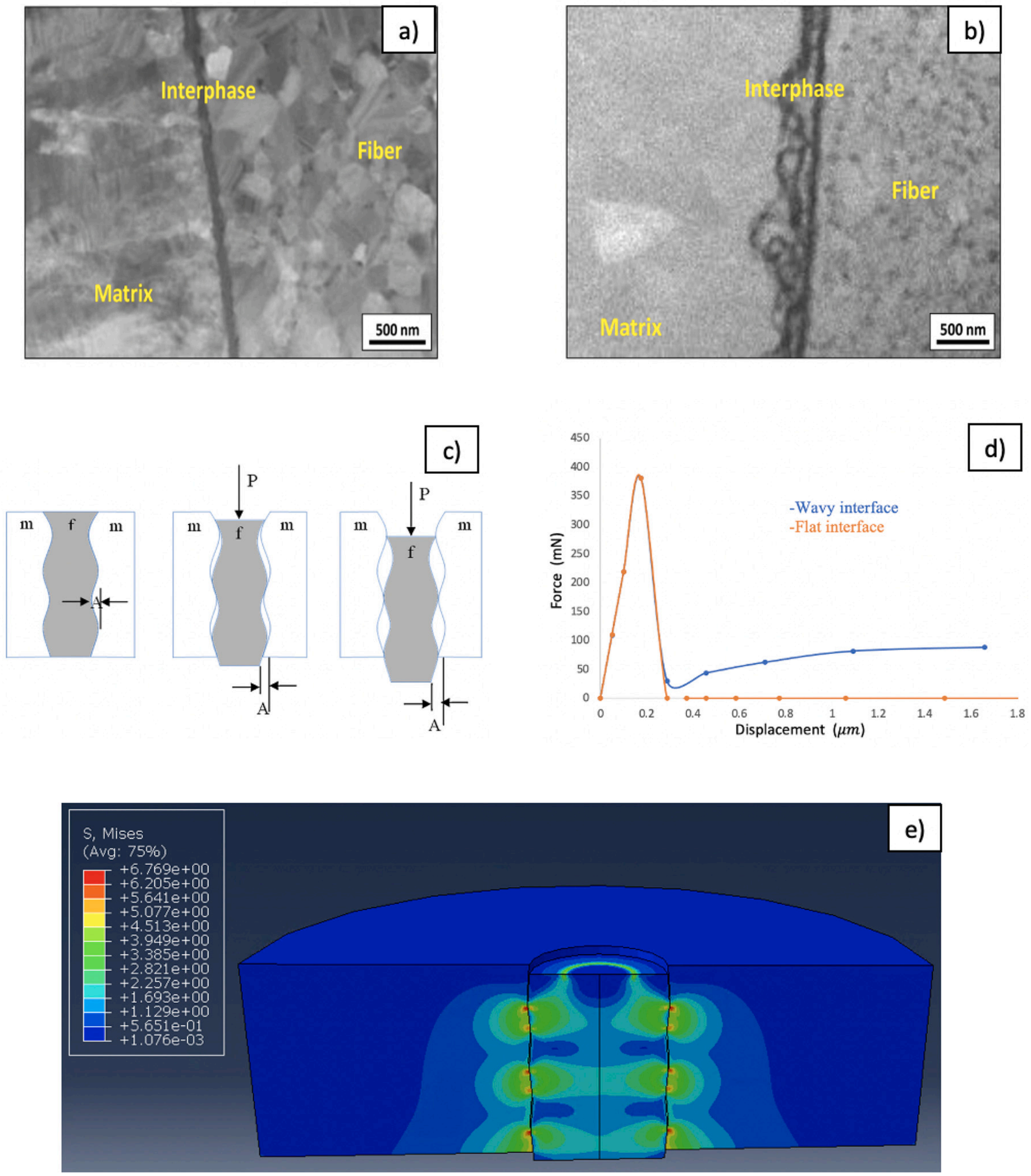

Fig. C.11. (a) STEM image of a single-layered 100 nm PyC interphase [11] similar to the fibers studied. (b) STEM image of a multi-layered PyC interphase [11] with high roughness. (c) Schematic representation of the effect of the fiber surface roughness on the interfacial shear stress [15]. (d) Force–displacement curve of push-out of fibers with the wavy and flat interface. (e) σ_{Mises} profile of FEM push-out simulation of fiber with a wavy interface.

$P_{fric}(FEM)$ = 82 mN (see the maximum force value after the peak in Fig. C.11d). Both methods show a good agreement with a difference of 23%. $P_{fric}(Fourier)$ was calculated with the following equation:

$$P_{fric} = C_{Fourier}\frac{\pi R E_{Fiber}}{\nu_{Fiber}}\left[\exp(2\mu\Lambda\nu_{Fiber}t/(RE_{Fiber})) - 1\right]$$

$$\text{where} \quad \Lambda = \frac{E_{\text{Fiber}}E_{\text{Matrix}}}{E_{\text{Matrix}}\left(1-\nu_{\text{Fiber}}\right)+E_{\text{Fiber}}\left(1+\nu_{\text{Matrix}}\right)} \qquad \text{(C.1)}$$

where E_i is Young's modulus, ν_i is Poisson's ratio, μ is the Coulomb's friction coefficient, R is the fiber radius (see the values of these magnitudes in Sections 4.1 and 4.2) and t = 13.3 μm is the fiber length minus the length of the fiber expelled due to the push-out. $C_{Fourier}$ = 40 nm was the maximum Fourier coefficient for the zigzag interface.

Although the results are satisfactory, the roughness profile is difficult to obtain in microscopic-sized fibers (~4 μm of radius and ~90 μm of length in the fibers of this article). In [15,43], the friction of microscopic-sized fibers is simulated using Coulomb friction and a constant fitting term:

$$\sigma_{fric} = \mu \cdot \sigma_n + \tau_0 \qquad \text{(C.2)}$$

The same method was followed in the simulations of this article, where τ_0 was not necessary to include, probably because was not comparable to Coulomb friction contribution.

The study of interface roughness requires a more comprehensive analysis for more irregular interfaces, and this preliminary modeling serves as a proof of concept that finite element simulations can be a suitable tool for such studies.

References

[1] Y. Katoh, L. Snead, C. Henager, T. Nozawa, T. Hinoki, A. Iveković, S. Novak, S. Gonzalez de Vicente, Current status and recent research achievements in SiC/SiC composites, J. Nucl. Mater. 455 (1) (2014) 387–397, Proceedings of the 16th International Conference on Fusion Reactor Materials (ICFRM-16).

[2] A. Ivekovic, S. Novak, G. Drazic, D. Blagoeva, S.G. de Vicente, Current status and prospects of SiCf/SiC for fusion structural applications, J. Eur. Ceram. Soc. 33 (10) (2013) 1577–1589.

[3] J.A. DiCarlo, N.P. Bansal, J. Lamon, Advances in SiC/SiC composites for aero-propulsion, 2014.

[4] E.A. Gulbransen, S.A. Jansson, The high-temperature oxidation, reduction, and volatilization reactions of silicon and silicon carbide, Oxid. Met. 4 (1972) 181–201.

[5] C. Carter Jr., R. David, J. Bentley, Kinetics and mechanisms of high-temperature creep in silicon carbide: I, reaction-bonded, J. Am. Ceram. Soc. 67 (6) (1984) 409–417.

[6] H. Kikuchi, R.K. Kalia, A. Nakano, P. Vashishta, P.S. Branicio, F. Shimojo, Brittle dynamic fracture of crystalline cubic silicon carbide (3C-SiC) via molecular dynamics simulation, J. Appl. Phys. 98 (10) (2005) 103524.

[7] E. Fitzer, D. Hegen, Chemical vapor deposition of silicon carbide and silicon nitride—Chemistry's contribution to modern silicon ceramics, Angew. Chem. Int. Ed. Engl. 18 (4) (1979) 295–304.

[8] A. Campbell, T. Burchell, 3.11 - Radiation effects in graphite, in: R.J. Konings, R.E. Stoller (Eds.), Comprehensive Nuclear Materials, second ed., Elsevier, 2020, pp. 398–436.

[9] J. Kabel, P. Hosemann, Y. Zayachuk, D.E.J. Armstrong, T. Koyanagi, Y. Katoh, C. Deck, Ceramic composites: A review of toughening mechanisms and demonstration of micropillar compression for interface property extraction, J. Mater. Res. 33 (4) (2018) 424–439.

[10] Y. Zayachuk, P. Karamched, C. Deck, P. Hosemann, D.E. Armstrong, Linking microstructure and local mechanical properties in SiC-SiC fiber composite using micromechanical testing, Acta Mater. 168 (2019) 178–189.

[11] A. Hussey, R. De Meyere, C. Deck, D. Armstrong, Y. Zayachuk, Statistically sound application of fiber push-out method for the study of locally non-uniform interfacial properties of SiC-SiC fiber composites, J. Eur. Ceram. Soc. 40 (4) (2020) 1052–1056.

[12] G. Lin, P. Geubelle, N. Sottos, Simulation of fiber debonding with friction in a model composite push-out test, Int. J. Solids Struct. 38 (46) (2001) 8547–8562.

[13] P. Lawrence, Some theoretical considerations of fibre pull-out from an elastic matrix, J. Mater. Sci. 135 (1972) 102817.

[14] F. Rebillat, J. Lamon, R. Naslain, E. Lara-Curzio, M.K. Ferber, T.M. Besmann, Interfacial bond strength in SiC/C/SiC composite materials, as studied by single-fiber push-out tests, J. Am. Ceram. Soc. 81 (4) (2005) 965–978.

[15] E. Buet, C. Sauder, D. Sornin, S. Poissonnet, J.-N. Rouzaud, C. Vix-Guterl, Influence of surface fibre properties and textural organization of a pyrocarbon interphase on the interfacial shear stress of SiC/SiC minicomposites reinforced with Hi-Nicalon S and Tyranno SA3 fibres, J. Eur. Ceram. Soc. 34 (2) (2014) 179–188.

[16] E. Buet, J. Braun, C. Sauder, Influence of texture and thickness of pyrocarbon coatings as interphase on the mechanical behavior of specific 2.5 D SiC/SiC composites reinforced with hi-nicalon S fibers, Coatings 12 (5) (2022) 573.

[17] C. Deck, H. Khalifa, B. Sammuli, T. Hilsabeck, C. Back, Fabrication of SiC–SiC composites for fuel cladding in advanced reactor designs, Prog. Nucl. Energy 57 (2012) 38–45, Nuclear Materials: Selected articles from the E-MRS 2011 Spring Meeting.

[18] Z. Ma, H. Zhao, X. Du, M. Zhou, X. Ma, C. Liu, L. Ren, Evaluation of nanoindentation load-depth curve of MEMS bridge structures by calculating the critical elastic-plastic bending deflections, Appl. Surf. Sci. 434 (2018) 1–10.

[19] W.B. Hillig, Melt infiltration approach to ceramic matrix composites, J. Am. Ceram. Soc. 71 (2) (1988) C–96–C–99.

[20] F.H. Gern, R. Kochendörfer, Liquid silicon infiltration: description of infiltration dynamics and silicon carbide formation, Composites A 28 (4) (1997) 355–364.

[21] L.L. Snead, T. Nozawa, Y. Katoh, T.-S. Byun, S. Kondo, D.A. Petti, Handbook of SiC properties for fuel performance modeling, J. Nucl. Mater. 371 (1) (2007) 329–377, Nuclear Fuels and Structural Materials 1.

[22] M. Sawan, N. Ghoniem, L. Snead, Y. Katoh, Damage production and accumulation in SiC structures in inertial and magnetic fusion systems, J. Nucl. Mater. 417 (1) (2011) 445–450, Proceedings of ICFRM-14.

[23] W. Gauthier, F. Pailler, J. Lamon, R. Pailler, Oxidation of silicon carbide fibers during static fatigue in air at intermediate temperatures, J. Am. Ceram. Soc. 92 (9) (2009) 2067–2073.

[24] K. Morishita, S. Ochiai, H. Okuda, T. Inshikawa, M. Sato, T. Inoue, Fracture toughness of a crystalline silicon carbide fiber (Tyranno-SA3), J. Am. Ceram. Soc. 89 (8) (2006) 2571–2576.

[25] R. De Meyere, L. Gale, S. Harris, I.M. Edmonds, T. Marrow, D. Armstrong, Optimizing the fiber push-out method to evaluate interfacial failure in SiC/BN/SiC ceramic matrix composites, J. Am. Ceram. Soc. 104 (6) (2021) 2741–2752.

[26] R. Wang, J. Han, J. Mao, D. Hu, X. Liu, X. Guo, A molecular dynamics based cohesive zone model for interface failure under monotonic tension of 3D four direction SiCf/SiC composites, Compos. Struct. 274 (2021) 114397.

[27] Z. Xia, J.W. Hutchinson, Mode II fracture toughness of a brittle adhesive layer, Int. J. Solids Struct. 31 (8) (1994) 1133–1148.

[28] R.J. Kerans, T.A. Parthasarathy, Theoretical analysis of the fiber pullout and pushout tests, J. Am. Ceram. Soc. 74 (7) (1991) 1585–1596.

[29] N. Chandra, H. Ghonem, Interfacial mechanics of push-out tests: theory and experiments, Composites A 32 (3) (2001) 575–584.

[30] M. Smith, ABAQUS/Standard User's Manual, Version 6.14, Dassault Systèmes Simulia Corp, United States, 2022.

[31] P.H. Geubelle, J.S. Baylor, Impact-induced delamination of composites: a 2D simulation, Composites B 29 (5) (1998) 589–602.

[32] J. Nelder, R. Mead, A simplex method for function minimization, Comput. J. 7 (1965) 308–313.

[33] S. Joglekar, Nelder-Mead Optimization technique, 2016, https://codesachin.wordpress.com/2016/01/16/nelder-mead-optimization/.

[34] S. Das, H. Yu, K. Mizohata, E. Tarleton, F. Hofmann, Modified deformation behavior of self-ion irradiated tungsten: A combined nano-indentation, HR-EBSD and crystal plasticity study, Int. J. Plast. 135 (2020) 102817.

[35] J. Kabel, Y. Yang, M. Balooch, C. Howard, T. Koyanagi, K. Terrani, Y. Katoh, P. Hosemann, Micro-mechanical evaluation of SiC-SiC composite interphase properties and debond mechanisms, Composites B 131 (2017) 173–183.

[36] M.-Y. He, J.W. Hutchinson, Crack deflection at an interface between dissimilar elastic materials, Int. J. Solids Struct. 25 (9) (1989) 1053–1067.

[37] N. Carrère, E. Martin, J. Lamon, The influence of the interphase and associated interfaces on the deflection of matrix cracks in ceramic matrix composites, Composites A 31 (11) (2000) 1179–1190.

[38] M. Sakai, R.C. Bradt, D. Fischbach, Fracture toughness anisotropy of a pyrolytic carbon, Mater. Sci. 21 (1986) 1491–1501.

[39] B. Malyshev, R. Salganik, The strength of adhesive joints using the theory of cracks, Int. J. Fract. 1 (1965) 114–128.

[40] M.R. Begley, J.W. Hutchinson, The Mechanics and Reliability of Films, Multilayers and Coatings, Cambridge University Press, United Kingdom, 2022.

[41] R. De Meyere, K. Song, et al., A novel trench fibre push-out method to evaluate interfacial failure in long fibre composites, J. Mater. Res. 36 (2021) 2305–2314.

[42] T.A. Parthasarathy, D.R. Barlage, P.D. Jero, R.J. Kerans, Effect of interfacial roughness parameters on the fiber pushout behavior of a model composite, J. Am. Ceram. Soc. 77 (12) (1994) 3232–3236.

[43] G. Alfano, E. Sacco, Combining interface damage and friction in a cohesive-zone model, Internat. J. Numer. Methods Engrg. 68 (5) (2006) 542–582.